UCLA
UCLA Previously Published Works

Title

Catalytic iron-carbene intermediate revealed in a cytochrome c carbene transferase

Permalink

https://escholarship.org/uc/item/8qn67140

Journal

Proceedings of the National Academy of Sciences of the United States of America, 115(28)

ISSN

0027-8424

Authors

Lewis, Russell D
Garcia-Borràs, Marc
Chalkley, Matthew J
et al.

Publication Date

2018-07-10

DOI

10.1073/pnas.1807027115

Peer reviewed

Catalytic iron-carbene intermediate revealed in a cytochrome *c* carbene transferase

Russell D. Lewis[a,1], Marc Garcia-Borràs[b,1], Matthew J. Chalkley[c], Andrew R. Buller[c,2], K. N. Houk[b,3], S. B. Jennifer Kan[c,3], and Frances H. Arnold[a,c,3]

[a]Division of Biology and Bioengineering, California Institute of Technology, Pasadena, CA 91125; [b]Department of Chemistry and Biochemistry, University of California, Los Angeles, CA 90095; and [c]Division of Chemistry and Chemical Engineering, California Institute of Technology, Pasadena, CA 91125

Contributed by Frances H. Arnold, May 31, 2018 (sent for review April 26, 2018; reviewed by Kara L. Bren and Ryan G. Hadt)

Recently, heme proteins have been discovered and engineered by directed evolution to catalyze chemical transformations that are biochemically unprecedented. Many of these nonnatural enzyme-catalyzed reactions are assumed to proceed through a catalytic iron porphyrin carbene (IPC) intermediate, although this intermediate has never been observed in a protein. Using crystallographic, spectroscopic, and computational methods, we have captured and studied a catalytic IPC intermediate in the active site of an enzyme derived from thermostable *Rhodothermus marinus* (*Rma*) cytochrome *c*. High-resolution crystal structures and computational methods reveal how directed evolution created an active site for carbene transfer in an electron transfer protein and how the laboratory-evolved enzyme achieves perfect carbene transfer stereoselectivity by holding the catalytic IPC in a single orientation. We also discovered that the IPC in *Rma* cytochrome *c* has a singlet ground state electronic state and that the protein environment uses geometrical constraints and noncovalent interactions to influence different IPC electronic states. This information helps us to understand the impressive reactivity and selectivity of carbene transfer enzymes and offers insights that will guide and inspire future engineering efforts.

carbene | reactive intermediate | heme | metalloenzyme | carbene transferase

Carbenes are formally neutral, divalent carbon species with two nonbonded electrons. They are typically reactive due to their incomplete octet electron configuration (1). Highly stabilized ("persistent") carbenes exist in biological systems, most notably as the deprotonated thiazolium group of thiamine in pyruvate oxidases (2). In contrast, reactive metal-carbenes have not been found in nature, despite their versatility and utility in chemical synthesis (3–5). Recent protein engineering efforts have revealed that heme proteins can catalyze a myriad of formal carbene transfer reactions, including alkene cyclopropanation (6–9), alkyne cyclopropenation and bicyclobutanation (10), and carbonyl olefination (11) as well as carbon–boron (12), –nitrogen (13), –silicon (14), and –sulfur (15) bond formation (Fig. 1). The proteins enable the heme center to make products that iron porphyrin alone does not (10, 12), and their genetically encoded structures direct selectivity that can be switched by evolution (6, 8–10, 12, 14), making it possible to create whole new biocatalytic pathways to important molecules.

By analogy to known transition metal-catalyzed reactions that use diazo reagents as carbene precursors (3–5), the emerging enzymatic carbene transfer activities of heme proteins are all thought to involve a reactive iron porphyrin carbene (IPC) intermediate; transfer of the carbene to a second substrate and product release regenerate the protein catalyst (6–15). Our current understanding of enzyme-catalyzed carbene transfer reactions comes primarily from experimental characterizations of model IPC compounds (16–21) and their computational studies (22–27). Determining the structures and properties of reactive intermediates is central to deciphering how enzymes enhance reaction rates and dictate selectivity (28), and recent mechanistic

studies of cyclopropanation enzymes (24, 26, 27) have also underscored the importance of the IPC intermediate and the need to characterize it within a protein scaffold.

Results and Discussion

Structural Characterization of Engineered Carbene Transferase, *Rhodothermus marinus* cytochrome *c* V75T M100D M103E.

Rhodothermus marinus (*Rma*) cytochrome c (cyt *c*) is an electron transfer protein [Protein Data Bank (PDB) ID code 3CP5] (29) previously engineered to catalyze the formation of carbon–silicon (14) and carbon–boron (12) bonds by inserting a reactive iron-carbene into the corresponding Si–H and B–H bonds of a silane or borane substrate. We set out to capture and characterize the IPC intermediate in *Rma* cyt *c* by turning to *Rma* cyt *c* V75T M100D M103E (TDE), a variant previously engineered to catalyze silylation reactions with high efficiency (14). *Rma* TDE was discovered after three rounds of site saturation mutagenesis and screening for enhanced activity, which resulted in amino acid substitutions V75T, M100D, and M103E. This protein is capable of catalyzing thousands of rounds of carbene transfer using ethyl 2-diazopropanoate (Me-EDA) (Fig. 2*A*) as a carbene precursor,

Fig. 1. The scope of laboratory-evolved biocatalytic carbene transfer reactions. Engineered heme proteins catalyze a broad range of abiological reactions with diazo reagents. These reactions are assumed to proceed through a catalytic IPC intermediate. X indicates porphyrin proximal ligand, usually serine or histidine. All published examples of heme-dependent carbene transfer enzymes accept diazo reagents having one or more electron-withdrawing groups (e.g., COOR, CF$_3$) as carbene precursors. The active resting state of the catalyst is Fe(II)-porphyrin.

presumably through the intermediacy of IPC **1** (Fig. 2*A*). To visualize the active site for carbene transfer, we obtained an X-ray crystal structure of *Rma* TDE at 1.47 Å (PDB ID code 6CUK) (*SI Appendix*, Table S1*A*). This structure reveals a pocket on the distal face of the heme created by the three mutations (Fig. 2*B*). In *Rma* TDE, the native distal methionine has been mutated to an aspartate (M100D), the α-carbon of which is displaced by 4.8 Å relative to its position in the wild-type structure (*SI Appendix*, Fig. S1). This displacement produces a cavity in the space previously occupied by the M100 sidechain and allows a water molecule (or hydroxide ion) to coordinate to the heme iron in the enzyme resting state. Overall, directed evolution created an entirely new active site in *Rma* TDE, where substrates bind, the carbene forms, and catalysis takes place.

Crystallographic Observation of an IPC in *Rma* TDE. To observe an IPC in the protein scaffold, crystals of *Rma* TDE were soaked with Me-EDA at room temperature for 30 min under air, reduced with sodium dithionite, and flash frozen in liquid nitrogen before diffraction. Under these conditions, we determined an X-ray crystal structure at 1.29 Å that shows a species bound to the iron porphyrin (PDB ID code 6CUN) that was not present in our previous structure of *Rma* TDE (PDB ID code 6CUK) (*SI Appendix*, Table S1*A*). We observed contiguous electron density from the iron porphyrin to an active site ligand, consistent with an enzymatic IPC intermediate, rather than iron-bound Me-EDA (Fig. 2*C*). The observed electron density is in agreement with a single carbene species in a single conformation (*SI Appendix*, section IIH), suggesting that this structure represents the dominant form of the IPC intermediate in solution during catalysis. The high occupancy of the carbene indicates that the rate of carbene formation greatly exceeds the rate of carbene decay in the absence of a second substrate, making the direct characterization of an enzymatic IPC intermediate possible.

The crystal structure of carbene-bound *Rma* TDE displays some similarities to previously studied small molecule IPC complexes. The Fe–C bond length of 1.9 Å is consistent with the previously determined structure of the IPC 1-methylimidazole-ligated mesotetrakis(pentafluorophenyl)porphyrin (TPFPP) diphenylcarbene, where the reported Fe–C bond length is 1.83 Å (20). The Fe–N (imidazole) bond length of 2.1 Å in the protein is

also consistent with that in the small molecule structure (2.17 Å) (20). Out-of-plane distortions, particularly ruffling distortions, are observed in both the imidazole-ligated TPFPP diphenylcarbene structure and the carbene-bound *Rma* TDE structure. Whereas the mean out-of-plane deviation for TPFPP diphenylcarbene was 1.03 Å (*SI Appendix*, Table S2), it is smaller for carbene-bound *Rma* TDE (0.6 Å; the deviation for *Rma* TDE alone is 0.7 Å). The difference in distortion between both *Rma* TDE structures is small, and both values are within the range reported for c-type cytochrome proteins (0.3–1.2 Å) (30). Ruffling is known to be the main distortion in these proteins and is thought to be induced by covalent attachment of the heme to the protein (31).

In contrast to what we observed in *Rma* TDE in the absence of Me-EDA, amino acid residues D100, T101, and D102 are unresolved in the carbene-bound *Rma* TDE structure, indicating that this loop region is flexible and the carbene is solvent accessible (Fig. 2*C*). The crystal structure also reveals close, nonpolar contacts between the iron-carbene and five amino acid sidechains (T75, M76, P79, I83, and M89 are 3.5–4.3 Å from the carbene) (Fig. 2*C*), suggesting that the active site is strongly hydrophobic, despite its solvent accessibility.

IPC Electronic Structure and Spectroscopy. When first proposed as a reactive enzyme intermediate, the IPC in cytochrome P450 was presented as analogous to oxoferryl intermediates found in the natural P450 catalytic cycle (6). This assignment was supported by the Fe(IV)-like Mössbauer parameters obtained for small molecule IPC complexes (20, 21, 32). However, Zhang and coworkers (24, 26, 27) have argued that IPCs are better described as Fe(II) closed shell singlets, lower in energy than the triplet states. Most recently, Shaik and coworkers (23) studied a model IPC complex and concluded that the lowest energy state for their IPC was an open shell singlet, best described as an $S = 1/2$ Fe(III) that is antiferromagnetically coupled to a carbene radical. Although the IPC open shell singlet is similar to the Fe(III)-superoxide electronic structure in heme oxygen binding (33), no experimental evidence has been published to support the relevance of an open shell singlet configuration in IPCs. Computational studies from both the Zhang group and the Shaik group suggest that the energy differences between electronic states are small (22–24, 27), and thus, the open shell singlet, closed shell singlet, and triplet states should all be considered plausible ground states for the IPC intermediate in the environment of an enzyme active site.

Encouraged by our success in capturing the IPC in the enzyme crystals, we sought to use spectroscopy to characterize the electronic structure of the IPC in *Rma* TDE. Under conditions similar to those where *Rma* TDE is catalytically active, we prepared solution samples of both *Rma* TDE and Me-EDA–treated *Rma* TDE and analyzed them with ultraviolet-visible (*SI Appendix*, Fig. S2), electron paramagnetic resonance (EPR), and Mössbauer spectroscopy. Neither sample gave EPR signals in either parallel (10 mW) or perpendicular (2 mW) mode at 4 K (*SI Appendix*, Fig. S3). While the absence of EPR signals under these conditions does not prove that the samples are diamagnetic, these results are consistent with our assignment of the resting enzyme and carbene-bound enzyme as low-spin species (vide infra). Mössbauer spectra of *Rma* TDE at 80 K were best fit as a single species with an isomer shift (∂_{Fe}) of 0.45 mm·s^{-1} and a quadrupole splitting ($|\Delta E_Q|$) of 1.18 mm·s^{-1} (*SI Appendix*, Fig. S4), consistent with an $S = 0$ low-spin Fe(II) resting-state species. This observation is in contrast to other Fe(II) hemes in proteins lacking an endogenous distal ligand to iron, which have been shown to favor high-spin ($S = 2$) states (34, 35). Mössbauer spectra of Me-EDA–treated *Rma* TDE at 80 K indicated the presence of a major species (88% abundance) and a minor species (12% abundance), the latter of which was assigned as ferrous *Rma* TDE. The major species was assigned as carbene-bound *Rma* TDE based on the Mössbauer parameters
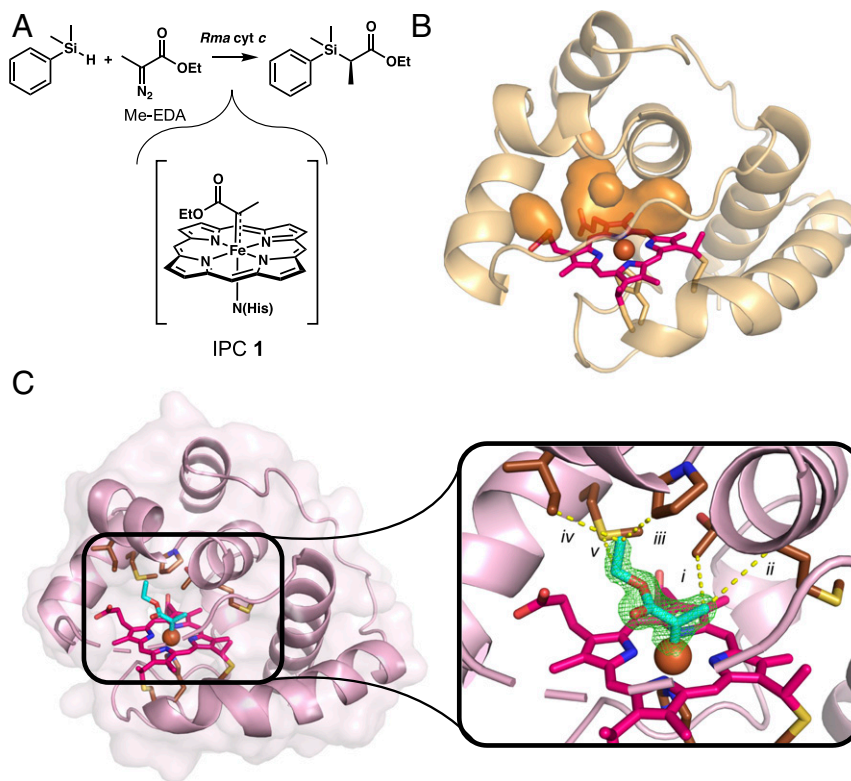
Fig. 2. Carbene transfer silylation reaction and structures of resting and carbene-bound *Rma* TDE. (*A*) The C–Si bond-forming reaction catalyzed by *Rma* cytochrome *c* proceeds via intermediate IPC **1**. (*B*) Mutations V75T, M100D, and M103E (*Rma* TDE) in *Rma* cytochrome *c* increased its carbene transfer activity (14). The crystal structure of *Rma* TDE with no Me-EDA bound (1.47 Å; PDB ID code 6CUK) reveals a cavity distal to the heme (orange surfaces) that is not present in wild-type *Rma* cyt *c*. (*C*) The crystal structure of carbene-bound *Rma* TDE (1.29 Å; PDB ID code 6CUN), with the carbene species in cyan. Residues D100, T101, and D102 are unresolved. (*Inset*) Omit map in green (F_O–F_C) of the carbene electron density contoured at 3σ. Interactions between the carbene and amino acid residues are shown with yellow lines. (*i*) T75, 3.7 Å. (*ii*) M76, 4.3 Å. (*iii*) P79, 3.5 Å. (*iv*) I83, 3.6 Å. (*v*) M89, 3.5 Å.

obtained ($\partial_{Fe} = 0.18$ mm·s^{-1}, $|\Delta E_Q| = 1.83$ mm·s^{-1}) and the lack of observed EPR signal (*SI Appendix*, Figs. S3 and S4). Thus, this reactive intermediate can be made in high yields and studied in both freeze-quenched solutions and crystals.

Computational Models of the IPC. The symmetric Mössbauer line shape of Me-EDA–treated *Rma* TDE and its lack of EPR signal suggested that this is an $S = 0$ species or an $S = 1$ species with a large zero-field splitting. To further differentiate these electronic states, we used density functional theory (DFT) to characterize model structures of IPC **1** in three possible electronic states. Our calculations showed that the closed shell singlet ($S = 0$) state was 8.8 kcal·mol^{-1} more stable than the triplet state ($S = 1$) and 1.0 kcal·mol^{-1} less stable than the open shell singlet (Fig. 3*A* and *SI Appendix*, Fig. S5). The geometrical features of the DFT-optimized structures also suggested that the IPC in *Rma* TDE exists as a singlet: the orientation of the ester group in the carbene-bound *Rma* TDE crystal structure is similar to that observed in the optimized closed shell and open shell singlet structures but distinctly different from the triplet state (Fig. 3*A*). The electronic structure of cytochrome proteins is known to correlate with heme ruffling (31, 36), and the singlet ground state is further supported by heme ruffling analysis (*SI Appendix*, Table S2): the ruffling out-of-plane distortion observed in the crystal structure of carbene-bound *Rma* TDE (0.5 Å) is more similar to that observed in the DFT-optimized closed shell singlet (0.401 Å) and open shell singlet (0.421 Å) states than in the triplet state (0.784 Å), where the heme is more distorted. While our DFT calculations suggested that the triplet state was energetically and geometrically unfavorable, the open shell and closed shell singlet

states are very close in energy and cannot be unambiguously assigned to IPC **1** (*SI Appendix*, Fig. S5). We also simulated the Mössbauer parameters of the open shell and closed shell singlet states but found that their predicted Mössbauer parameters were within experimental error of the observed values (*SI Appendix*, Fig. S4*E*). Spectroscopy and theory indicate that carbene-bound *Rma* TDE is a ground-state singlet.

The DFT models suggest that the observed end-on carbene is thermodynamically more stable than the alternative (Fe, N)-bridged carbene, which also requires a large distortion of the porphyrin that is difficult to attain for the covalently ligated heme in cyt *c* proteins (*SI Appendix*, Fig. S6). This is in contrast to the thiolate-ligated IPC computationally studied by Shaik and coworkers (23), where the (Fe, N)-bridged mode was found to be thermodynamically favored. Small molecule (Fe, N)-bridged IPCs have been synthesized and crystallized (17–19, 25); their experimental characterizations are distinct from that of end-on IPCs. As far as we know, (Fe, N)-bridged carbenes are not active intermediates in carbene transfer reactions (37).

Computational Modeling of the IPC Enzymatic Intermediate. We next used molecular dynamics (MD) to understand how the protein scaffold of *Rma* TDE affects the conformation and properties of the IPC intermediate. MD simulations were performed on singlet IPC **1** docked into *Rma* TDE (PDB ID code 6CUK) using various IPC **1** conformations as starting points and explicit water as solvent. MD trajectories revealed that, regardless of the initial carbene orientation, the IPC converges to a single well-defined orientation (Fig. 3*B* and *SI Appendix*, Fig. S7). This conformation is remarkably similar to that observed in the carbene-bound
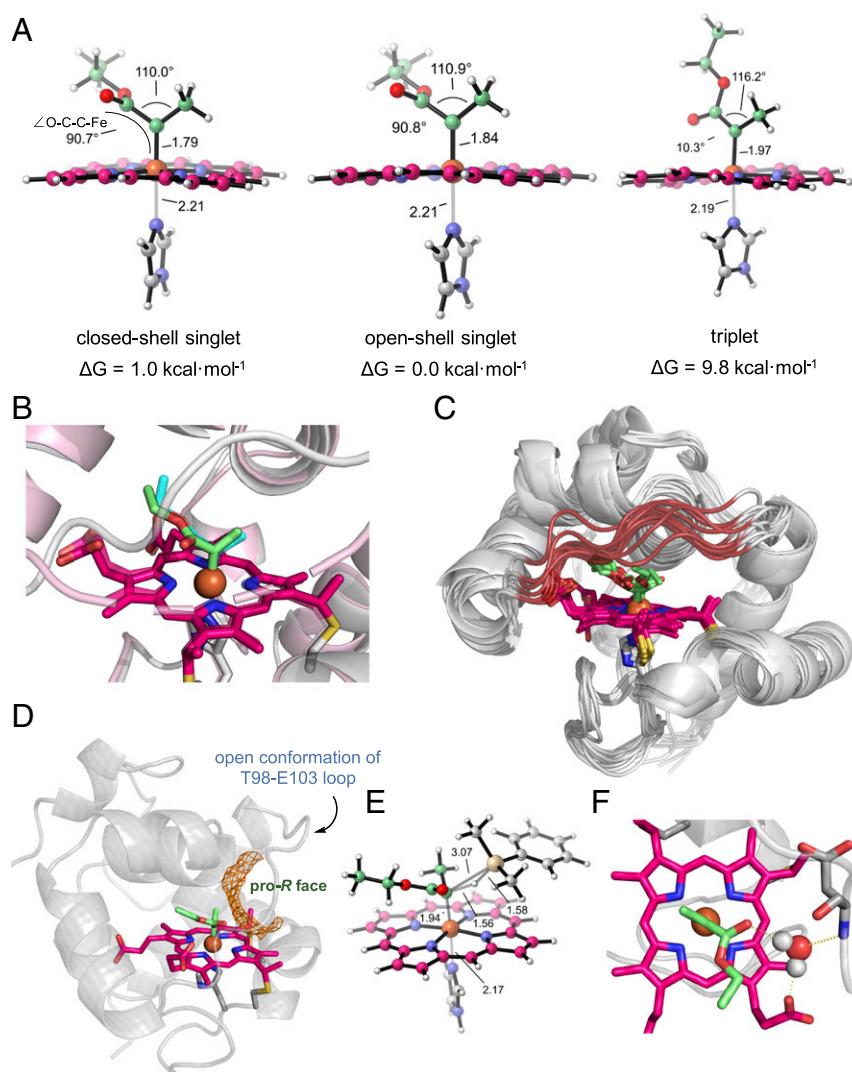
Fig. 3. Computational models of carbene-bound *Rma* TDE. (*A*) DFT optimized structures of model IPC **1** in the closed shell singlet, open shell singlet, and triplet electronic states. DFT calculations predict that the singlet state is 8.8 kcal·mol^{-1} more stable than the triplet state, which is consistent with previously characterized small molecule IPCs. The calculated Fe–C bond lengths are 1.79, 1.84, and 1.97 Å for the closed shell singlet, open shell singlet, and triplet, respectively. The Fe–N (imidazole) bond lengths are 2.21, 2.21, and 2.19 Å, respectively. These numbers are within experimental error of the lengths observed in the carbene-bound *Rma* TDE crystal structure, where the Fe–C bond length is 1.9 Å and the Fe–N bond length is 2.1 Å. (*B*) Overlay of the carbene-bound *Rma* TDE crystal structure with a QM/MM-optimized structure of carbene-bound *Rma* TDE. QM/MM structure: protein scaffold is gray, and carbene is green. Crystal structure (PDB ID code 6CUN): protein scaffold is light pink, and carbene is cyan. The preferred carbene conformation determined by MD simulations and QM/MM calculations is almost identical to that determined by X-ray crystallography. (*C*) Overlay of 10 representative snapshots obtained from 1,000 ns of MD simulation on the carbene-bound *Rma* TDE. Simulations show that the active site front loop (residues 98–103; highlighted in red) is highly flexible, switching between "open" and "closed" conformations. Despite the front loop's high flexibility, the carbene is stabilized in a single major conformation (*SI Appendix*, Fig. S7). (*D*) Snapshot obtained from an MD trajectory on carbene-bound *Rma* TDE with the front loop in the open conformation, showing that the carbene pro-*R* face is solvent exposed. Solvent-accessible area is showed in orange. (*E*) DFT-optimized structure of the lowest-energy pro-*R* transition state (closed shell singlet state) for Si–H insertion with IPC **1** (*SI Appendix*, Fig. S8). (*F*) A representative view of an MD snapshot on carbene-bound *Rma* TDE showing interactions between the bridging water with the heme carboxylate, the carbene carbonyl, and the amide bond of residue D100. Hydrogen-bonding interactions with the carbene have been shown to affect the stability of IPCs (25, 27, 37).

Rma cyt *c* crystal structure, indicating the catalytic relevance of the latter in solution (Fig. 3*B*). Furthermore, MD simulations highlighted the flexibility of the active site front loop (T98-E103) (Fig. 3*C*), favoring an "open" conformation where the IPC is solvent exposed and accessible to substrates with pro-*R* facial selectivity, while keeping the pro-*S* face inaccessible (Fig. 3*D*). This high degree of loop flexibility is consistent with the unresolved residues (D100–D102) observed in the carbene-bound *Rma* TDE crystal structure (Fig. 2*C*). To further investigate the protein's enantiopreference, we performed DFT calculations to characterize the intrinsic geometric features of the pro-*R* transition

state for carbene Si–H insertion using a truncated computational model and dimethylphenylsilane as substrate (Fig. 3*E* and *SI Appendix*, Fig. S8). When comparing the lowest energy-optimized pro-*R* transition state with the most populated structure of carbene-bound *Rma* TDE, the space made available when *Rma* TDE is in its open conformation provides a perfect fit for the silane substrate (Fig. 3 *D* and *E* and *SI Appendix*, Fig. S8). However, the pro-*S* transition state could only take place when the IPC is rotated away from its preferred conformation, which is disfavored by the active site of *Rma* TDE. Thus, in *Rma* TDE-catalyzed carbon–silicon bond-forming reactions, the protein dictates substrate

approach to the IPC intermediate from the pro-*R* face, which on carbene transfer to the Si–H bond of the silane substrate, gives *R*-configured organosilicon products exclusively as observed experimentally (>99% enantiomeric excess) (14).

MD simulations also revealed the presence of a water molecule that forms persistent hydrogen bonds bridging one of the heme carboxylate groups and the carbonyl group of the carbene (Fig. 3*E*). This water molecule is highly conserved, with its position further stabilized by polar contacts with the front loop residues. In the carbene-bound *Rma* TDE crystal structure, this bridging water was not observed but was likely obscured due to its proximity to the unresolved residues D100–D102. Hydrogen bonding is known to affect the electronic structure and stability of IPC intermediates (25, 27, 37). In view of this, we designed a truncated computational model of an IPC–water complex, and through DFT calculations, we found that the H-bonding water molecule stabilizes the carbene complex by about 7 kcal·mol^{-1} in its closed shell singlet state. This stabilizing effect is more substantial on the closed shell singlet than on the open shell singlet or triplet states, contributing to determining the preferred conformation adopted by the IPC in the protein (*SI Appendix*, Fig. S9). Hybrid quantum mechanics/molecular mechanics (QM/MM) calculations showed that, within *Rma* TDE, the singlet–triplet energy gap of the hydrogen-bonded IPC increases by 2.9 kcal·mol^{-1} (8.8 kcal·mol^{-1} in the truncated model, 11.7 kcal·mol^{-1} when considering the full system) (*SI Appendix*, Fig. S10). This significant destabilization of the radical triplet state is largely due to conformational restraints imposed by the protein active site and the bridging water: to minimize steric clash with the P79 and I83 sidechains, the carbene ester is forced to adopt a conformation parallel to the heme, which is intrinsically preferred by the closed shell and open shell singlet states but disfavors the radical triplet state, as this conformation cannot stabilize the unpaired electron in the carbene *p* orbital by the adjacent ester. Thus, mediated by amino acid residues and an ordered water, the active site of *Rma* TDE imposes multiple conformational restraints on the IPC intermediate to stabilize the closed shell singlet state and disfavor the presence of carbene radicals.

Summary and Conclusions

In conclusion, characterization of a catalytically active IPC intermediate inside the active site of an enzyme has provided a foundation from which to study enzyme-catalyzed carbene transfer reactions and explain the reactivity and selectivity of *Rma* TDE-catalyzed carbene transfer. Structural characterization of the *Rma* TDE enzyme showed that the three mutations introduced during directed evolution led to dramatic changes in a loop distal to the heme and generated a protein structure preorganized for substrate binding and IPC formation. The experimental IPC structure and computational modeling showed that *Rma* TDE stabilizes a single conformation of the IPC that gives the enzyme complete stereoselectivity control during carbene transfer. The conformational restraints imposed by the enzyme also favor the formation of a singlet iron-carbene. This convergent approach to characterizing the emerging family of carbene transferases enables informed engineering that will enhance the generality and utility of these powerful catalysts.

Materials and Methods

Detailed experimental methods are presented in *SI Appendix*.

Cloning, Expression, and Purification of *Rma* TDE. The gene encoding *Rma* TDE was obtained as a gBlock and cloned into pET22b(+). Expression was performed in HyperBroth (AthenaES) using *Escherichia coli* BL21 *E. cloni* EXPRESS (Lucigen). ^{57}Fe-labeled protein was produced using defined media supplemented with ^{57}Fe. *Rma* TDE was purified via a HisTrap HP column (GE Healthcare).

Crystallography. Crystals of *Rma* TDE were grown using the sitting drop vapor diffusion method and were cryoprotected before diffraction at the Stanford Synchrotron Radiation Lightsource on beamline 12–2. Carbene-bound crystals of *Rma* TDE were prepared by soaking preformed crystals with concentrated solutions of Me-EDA and sodium dithionite. Structures were determined by molecular replacement, and models were built using standard procedures.

EPR Spectroscopy. EPR spectra were recorded on a Bruker EMX X-band CW-EPR spectrometer using Bruker Win-EPR software (version 3.0). Data were collected in parallel mode with a power of 10 mW and in perpendicular mode with a power of 2 mW, both at 4 K. Samples of *Rma* TDE were prepared under anaerobic conditions in the presence of sodium dithionite before flash freezing with liquid nitrogen.

Mössbauer Spectroscopy. Mössbauer spectra were recorded using a spectrometer from SEE Co., and data analysis was performed using the WMOSS program. Solution samples of ^{57}Fe-labeled *Rma* TDE were prepared under anaerobic conditions in the presence of sodium dithionite before flash freezing with liquid nitrogen. Samples were stored under liquid nitrogen until being mounted on the cryostat, and data were recorded at 77 K.

DFT Calculations. DFT calculations were carried out using Gaussian09 (38) and Gaussian16 (39) using a truncated model. Geometry optimizations and frequency calculations were performed using (U)B3LYP (40–42) functional with the SDD basis set for iron and 6–31G(d) on all other atoms and within the conductor-like polarizable continuum model (CPCM) (diethyl ether, ε = 4) (43, 44) to have an estimation of the dielectric permittivity in the enzyme active site. Enthalpies and entropies were calculated for 1 atm and 298.15 K. A correction to the harmonic oscillator approximation was also applied to the entropy calculations by raising all frequencies below 100 cm^{-1} to 100 cm^{-1} (45, 46). Single-point energy calculations were performed using the dispersion-corrected functional (U)B3LYP-D3(BJ) (47, 48) with the Def2TZVP basis set on all atoms and with CPCM (diethyl ether, ε = 4). All energy values discussed in the manuscript correspond to the quasiharmonic corrected Gibbs energies (ΔG-qh) at (U)B3LYP-D3(BJ)/Def2TZVP/PCM(diethyl ether)//(U)B3LYP/6–31G(d)+SDD(Fe)/PCM(diethyl ether) level if not otherwise noted. Further descriptions and details of the methodology are provided in *SI Appendix*.

Hybrid QM/MM Calculations. QM/MM calculations within the ONIOM approach (49, 50) were carried out using Gaussian09 (38). Geometry optimizations were performed using (U)B3LYP (40–42) functional in combination with the SDD basis set for iron and 6–31G(d) on all other atoms and AmberFF14Sb force field (51) using a mechanical embedding scheme. Stationary points were verified as minima by a vibrational frequency analysis, thermal corrections were calculated for 1 atm and 298.15 K, and a correction to the harmonic oscillator approximation was included as described above. Single-point energy calculations were performed at the (U)B3LYP/Def2TZVP:AmberFF14Sb level and using an electrostatic embedding scheme. Snapshots for QM/MM calculations were obtained from classical MD trajectories. Further descriptions and details of the methodology are provided in *SI Appendix*.

MD Simulations. MD simulations were performed using the GPU code (pmemd) (52) of the AMBER 16 package (53). Parameters for the carbene-bound IPC were generated within the antechamber and MCPB.py (54) modules in AMBER16 package using the general AMBER force field (gaff) (55), with partial charges set to fit the electrostatic potential generated at the B3LYP/6–31G(d) level by the RESP model (56). Protonation states of protein residues were predicted using H++ server. Each protein was immersed in a preequilibrated truncated cuboid box with a 10-Å buffer of TIP3P (57) water molecules using the leap module, and the systems were neutralized by addition of explicit counterions (Na$^+$ and Cl$^-$). All subsequent calculations were done using the widely tested Stony Brook modification of the Amber14 force field (ff14sb) (58). After minimization, heating, and equilibration of the system (*SI Appendix* has a full description of the protocol used), production trajectories were then run for 1,000 ns (1 μs). The obtained trajectories were processed and analyzed using the cpptraj (58) module from Ambertools utilities.

1. Bourissou D, Guerret O, Gabbaï FP, Bertrand G (2000) Stable carbenes. *Chem Rev* 100: 39–92.
2. Meyer D, Neumann P, Ficner R, Tittmann K (2013) Observation of a stable carbene at the active site of a thiamin enzyme. *Nat Chem Biol* 9:488–490.
3. Kornecki KP, et al. (2013) Direct spectroscopic characterization of a transitory dirhodium donor-acceptor carbene complex. *Science* 342:351–354.
4. Doyle MP (1986) Catalytic methods for metal carbene transformations. *Chem Rev* 86: 919–939.
5. Ford A, et al. (2015) Modern organic synthesis with α-diazocarbonyl compounds. *Chem Rev* 115:9981–10080.
6. Coelho PS, Brustad EM, Kannan A, Arnold FH (2013) Olefin cyclopropanation via carbene transfer catalyzed by engineered cytochrome P450 enzymes. *Science* 339: 307–310.
7. Bordeaux M, Tyagi V, Fasan R (2015) Highly diastereoselective and enantioselective olefin cyclopropanation using engineered myoglobin-based catalysts. *Angew Chem Int Ed Engl* 54:1744–1748.
8. Gober JG, et al. (2016) Mutating a highly conserved residue in diverse cytochrome P450s facilitates diastereoselective olefin cyclopropanation. *ChemBioChem* 17: 394–397.
9. Knight AM, et al. (2018) Diverse engineered heme proteins enable stereodivergent cyclopropanation of unactivated alkenes. *ACS Cent Sci* 4:372–377.
10. Chen K, Huang X, Kan SBJ, Zhang RK, Arnold FH (2018) Enzymatic construction of highly strained carbocycles. *Science* 360:71–75.
11. Weissenborn MJ, et al. (2016) Enzyme-catalyzed carbonyl olefination by the *E. coli* protein YfeX in the absence of phosphines. *ChemCatChem* 8:1636–1640.
12. Kan SBJ, Huang X, Gumulya Y, Chen K, Arnold FH (2017) Genetically programmed chiral organoborane synthesis. *Nature* 552:132–136.
13. Wang ZJ, Peck NE, Renata H, Arnold FH (2014) Cytochrome P450-catalyzed insertion of carbenoids into N-H bonds. *Chem Sci (Camb)* 5:598–601.
14. Kan SBJ, Lewis RD, Chen K, Arnold FH (2016) Directed evolution of cytochrome *c* for carbon-silicon bond formation: Bringing silicon to life. *Science* 354:1048–1051.
15. Tyagi V, Bonn RB, Fasan R (2015) Intermolecular carbene S-H insertion catalysed by engineered myoglobin-based catalysts. *Chem Sci (Camb)* 6:2488–2494.
16. Mansuy D, et al. (1978) Dichlorocarbene complexes of iron(II)-porphyrins-crystal and molecular structure of Fe(TPP)(CCl2)(H2O). *Angew Chem Int Ed Engl* 17:781–782.
17. Chevrier B, Weiss R, Lange M, Chottard JC, Mansuy D (1981) An iron(III)-porphyrin complex with a vinylidene group inserted into an iron-nitrogen bond: Relevance to the structure of the active oxygen complex of catalase. *J Am Chem Soc* 103: 2899–2901.
18. Olmstead MM, Cheng RJ, Balch AL (1982) X-ray crystallographic characterization of an iron porphyrin with a vinylidene carbene inserted into an iron-nitrogen bond. *Inorg Chem* 21:4143–4148.
19. Artaud I, Gregoire P, Leduc P, Mansuy D (1990) Formation and fate of iron-carbene complexes in reactions between a diazoalkane and iron-porphyrins: Relevance to the mechanism of formation of N-substituted hemes in cytochrome P-450 dependent oxidation of sydnones. *J Am Chem Soc* 112:6899–6905.
20. Li Y, Huang JS, Zhou ZY, Che CM, You XZ (2002) Remarkably stable iron porphyrins bearing nonheteroatom-stabilized carbene or (alkoxycarbonyl)carbenes: Isolation, X-ray crystal structures, and carbon atom transfer reactions with hydrocarbons. *J Am Chem Soc* 124:13185–13193.
21. Liu Y, et al. (2017) Electronic configuration and ligand nature of five-coordinate iron porphyrin carbene complexes: An experimental study. *J Am Chem Soc* 139:5023–5026.
22. Khade RL, et al. (2014) Iron porphyrin carbenes as catalytic intermediates: Structures, Mössbauer and NMR spectroscopic properties, and bonding. *Angew Chem Int Ed Engl* 53:7574–7578.
23. Sharon DA, Mallick D, Wang B, Shaik S (2016) Computation sheds insight into iron porphyrin carbenes' electronic structure, formation, and N-H insertion reactivity. *J Am Chem Soc* 138:9597–9610.
24. Wei Y, Tinoco A, Steck V, Fasan R, Zhang Y (2018) Cyclopropanations via heme carbenes: Basic mechanism and effects of carbene substituent, protein axial ligand, and porphyrin substitution. *J Am Chem Soc* 140:1649–1662.
25. Tatsumi K, Hoffmann R (1981) Metalloporphyrins with unusual geometries. 2. Slipped and skewed bimetallic structures, carbene and oxo complexes, and insertions into metal-porphyrin bonds. *Inorg Chem* 20:3771–3784.
26. Khade RL, Zhang Y (2015) Catalytic and biocatalytic iron porphyrin carbene formation: Effects of binding mode, carbene substituent, porphyrin substituent, and protein axial ligand. *J Am Chem Soc* 137:7560–7563.
27. Khade RL, Zhang Y (2017) C-H insertions by iron porphyrin carbene: Basic mechanism and origin of substrate selectivity. *Chemistry* 23:17654–17658.
28. Rittle J, Green MT (2010) Cytochrome P450 compound I: Capture, characterization, and C-H bond activation kinetics. *Science* 330:933–937.
29. Stelter M, et al. (2008) A novel type of monoheme cytochrome *c*: Biochemical and structural characterization at 1.23 A resolution of *rhodothermus marinus* cytochrome *c*. *Biochemistry* 47:11953–11963.
30. Graves AB, Graves MT, Liptak MD (2016) Measurement of heme ruffling changes in MhuD using UV-vis spectroscopy. *J Phys Chem B* 120:3844–3853.
31. Kleingardner JG, Bren KL (2015) Biological significance and applications of heme *c* proteins and peptides. *Acc Chem Res* 48:1845–1852.
32. English DR, Hendrickson DN, Suslick KS (1983) Mössbauer spectra of oxidized iron porphyrins. *Inorg Chem* 22:367–368.
33. Wilson SA, et al. (2013) X-ray absorption spectroscopic investigation of the electronic structure differences in solution and crystalline oxyhemoglobin. *Proc Natl Acad Sci USA* 110:16333–16338.
34. Ran Y, et al. (2010) Spectroscopic identification of heme axial ligands in HtsA that are involved in heme acquisition by Streptococcus pyogenes. *Biochemistry* 49:2834–2842.
35. Engler N, Prusakov V, Ostermann A, Parak FG (2003) A water network within a protein: Temperature-dependent water ligation in H64V-metmyoglobin and relaxation to deoxymyoglobin. *Eur Biophys J* 31:595–607.
36. Liptak MD, Wen X, Bren KL (2010) NMR and DFT investigation of heme ruffling: Functional implications for cytochrome *c*. *J Am Chem Soc* 132:9753–9763.
37. Dzik WI, Xu X, Zhang XP, Reek JNH, de Bruin B (2010) 'Carbene radicals' in Co(II)(por)-catalyzed olefin cyclopropanation. *J Am Chem Soc* 132:10891–10902.
38. Frisch MJ, et al. (2009) Gaussian 09, Revision A.02 (Gaussian Inc., Wallingford, CT).
39. Frisch MJ, et al. (2016) Gaussian 16, Revision B.01 (Gaussian, Inc., Wallingford, CT).
40. Becke AD (1988) Density-functional exchange-energy approximation with correct asymptotic behavior. *Phys Rev A Gen Phys* 38:3098–3100.
41. Becke AD (1993) Density-functional thermochemistry. III. The role of exact exchange. *J Chem Phys* 98:5648–5652.
42. Lee C, Yang W, Parr RG (1988) Development of the Colle-Salvetti correlation-energy formula into a functional of the electron density. *Phys Rev B Condens Matter* 37: 785–789.
43. Barone V, Cossi M (1998) Quantum calculation of molecular energies and energy gradients in solution by a conductor solvent model. *J Phys Chem A* 102:1995–2001.
44. Cossi M, Rega N, Scalmani G, Barone V (2003) Energies, structures, and electronic properties of molecules in solution with the C-PCM solvation model. *J Comput Chem* 24:669–681.
45. Ribeiro RF, Marenich AV, Cramer CJ, Truhlar DG (2011) Use of solution-phase vibrational frequencies in continuum models for the free energy of solvation. *J Phys Chem B* 115:14556–14562.
46. Zhao Y, Truhlar DG (2008) Computational characterization and modeling of buckyball tweezers: Density functional study of concave-convex pi...pi interactions. *Phys Chem Chem Phys* 10:2813–2818.
47. Grimme S, Ehrlich S, Goerigk L (2011) Effect of the damping function in dispersion corrected density functional theory. *J Comput Chem* 32:1456–1465.
48. Grimme S, Antony J, Ehrlich S, Krieg H (2010) A consistent and accurate *ab initio* parametrization of density functional dispersion correction (DFT-D) for the 94 elements H-Pu. *J Chem Phys* 132:154104.
49. Dapprich S, Komáromi I, Byun KS, Morokuma K, Frisch MJ (1999) A new ONIOM implementation in Gaussian98. Part I. The calculation of energies, gradients, vibrational frequencies and electric field derivatives. *J Mol Struct THEOCHEM* 461–462:1–21.
50. Chung LW, et al. (2015) The ONIOM method and its applications. *Chem Rev* 115: 5678–5796.
51. Maier JA, et al. (2015) ff14SB: Improving the accuracy of protein side chain and backbone parameters from ff99SB. *J Chem Theory Comput* 11:3696–3713.
52. Salomon-Ferrer R, Götz AW, Poole D, Le Grand S, Walker RC (2013) Routine microsecond molecular dynamics simulations with AMBER on GPUs. 2. Explicit solvent particle mesh Ewald. *J Chem Theory Comput* 9:3878–3888.
53. Case DA, et al. (2016) *Amber 16* (University of California, San Francisco).
54. Li P, Merz KM, Jr (2016) MCPB.py: A python based metal center parameter builder. *J Chem Inf Model* 56:599–604.
55. Wang J, Wolf RM, Caldwell JW, Kollman PA, Case DA (2004) Development and testing of a general amber force field. *J Comput Chem* 25:1157–1174.
56. Bayly CI, Cieplak P, Cornell W, Kollman PA (1993) A well-behaved electrostatic potential based method using charge restraints for deriving atomic charges: The RESP model. *J Phys Chem* 97:10269–10280.
57. Jorgensen WL, Chandrasekhar J, Madura JD, Impey RW, Klein ML (1983) Comparison of simple potential functions for simulating liquid water. *J Chem Phys* 79:926–935.
58. Roe DR, Cheatham TE, 3rd (2013) PTRAJ and CPPTRAJ: Software for processing and analysis of molecular dynamics trajectory data. *J Chem Theory Comput* 9:3084–3095.

BIOCHEMISTRY